

COMPARISON OF RANS MODELING WITH DNS AND EXPERIMENTAL DATA FOR A CONVERGING-DIVERGING NOZZLE AND A ROTATING CYLINDER ELECTRODE

C. JACOBS¹, Z. QIN² and K. BREMHORST¹

¹ Division of Mechanical Engineering, The University of Queensland, Brisbane, QLD, 4072, AUSTRALIA

² CRC –Mining, The University of Queensland, Brisbane, QLD, 4072, AUSTRALIA

ABSTRACT

Water flow through a convergent-divergent nozzle used for jet cutters is simulated with five two-equation turbulence models. Flow separation within the nozzle leads to two distinctly different types of behaviour for mean velocity along the nozzle. The realizable $k-\epsilon$ and the RNG $k-\epsilon$ models are found to produce generally similar results but which differ significantly from the $k-\omega$ based models. The standard $k-\epsilon$ model predicts pressure inside the throat of the nozzle well below that of the other models. Except for the standard $k-\epsilon$ model, all predict mass flow rates which agree with experimental values.

Further simulations involved the Rotating Cylinder Electrode (RCE). The Spalart-Allmaras, $k-\epsilon$ and $k-\omega$ models were used to predict the near-wall flow properties. It was found that the $k-\epsilon$ models with enhanced wall treatment predicted the near-wall flow conditions better than the $k-\omega$ models, however all models failed to accurately predict the near-wall turbulence dissipation rate. Wall shear stress values for all models were well below those predicted by direct numerical simulation.

NOMENCLATURE

k	turbulence kinetic energy (m^2/s^2)
u^*	friction velocity (m/s)
u^+	non-dimensional velocity based on u^*
x	axial coordinate relative to nozzle exit
y^+	non-dimensional radial distance
ϵ	turbulence dissipation rate (m^2/s^3)
ν	kinematic viscosity (m^2/s)
τ_w	wall shear stress (Pa)
ω	specific turbulence dissipation rate (s^{-1})

INTRODUCTION

Water at sufficiently high pressure when forced through a converging-diverging nozzle, can lead to cavitation. This characteristic is made use of in cavitating water jets for rock cutting (Meyer et al., 1999, Erdmann, 1978, Yanaida, 1985, Okumura et al, 1999, Terasaki et al, 1999, Qin, 2004). Whether or not cavitation occurs in a water jet depends strongly upon the pressure along the jet flow (Brennen, 1995, Lichtarowicz et al., 1999, Plesset and Prosperetti, 1977). To predict this pressure variation, one has to go beyond simple application of Bernoulli's equation. In this paper $k-\epsilon$ and $k-\omega$ two-equation

turbulence models are explored by comparison of simulations and measurements.

The Rotating Cylinder Electrode (RCE) is one of the most widely used methods of producing turbulent flow in laboratory based corrosion studies. The RCE tested consists of a concentric inner rotating cylinder of 10mm radius and an outer stationary cylinder of radius 70mm. The aim of the current work is to compare the results of two-dimensional Reynolds averaged Navier-Stokes (RANS) models for this geometry to the Direct Numerical Simulation (DNS) of Hwang et al. (2005) and the experimental work of Silverman (1988), Gabe (1974), Gabe and Walsh (1983).

SIMULATION OF CAVITATING WATER JET CUTTERS PRODUCED BY A CONVERGENT-DIVERGENT NOZZLE

Geometry Setup and Solution Domain

The simulations are based on the nozzle of Figure 1 and the cavitation cell of Figure 2. The cavitation cell has a diameter of 60mm, an annular outlet of 2mm width with the nozzle and a piece of pipe connected to the nozzle at the upstream inlet. The water jet enters through the converging-diverging nozzle into the cell which is kept at a constant pressure.

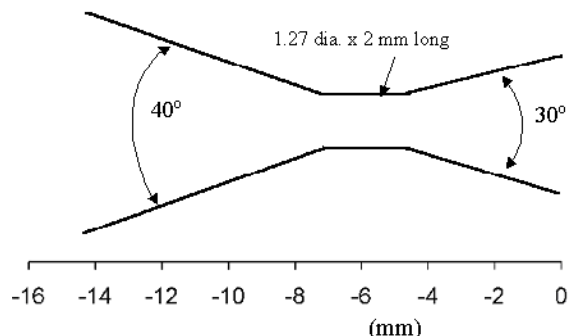


Figure 1: Convergent-divergent nozzle used in simulations

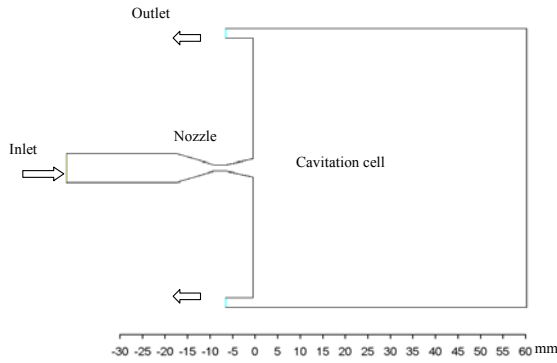


Figure 2: CFD modelled cavitation cell and nozzle

Flow Equations and their Solution

The mass conservation and Reynolds averaged Navier-Stokes equations were solved with the commercial software FLUENT (Version 6) with the standard, the RNG (renormalization group) and realizable $k-\epsilon$ models and the standard and shear stress transport (SST) $k-\omega$ models. The domain was discretised in GAMBIT (a software package attached to the FLUENT). Axisymmetry was assumed in the cell and for the nozzle geometry so that only half of the geometry was discretised. The boundary conditions are listed in Table 1.

Inlet pressure	10.2 MPa
Inlet temperature	300 K
Inlet turbulence intensity	4.5 %
Inlet hydraulic diameter	6.5 mm
Outlet pressure	6 MPa
Outlet temperature	300 K
Outlet turbulence intensity	4.5 %
Outlet hydraulic diameter	21 mm
Wall roughness height	0.0016 mm

Table 1: Boundary conditions for simulation

To assess the dependence of the simulation results on the mesh discretization, calculations were repeated for different mesh schemes. Further details of these tests are available in Qin (2004).

Results for Different Turbulence Models

From Figure 3 it can be seen that differences appear amongst the various models predominantly in the throat portion of the nozzle. The pressure reduction in the throat leads to cavitation bubbles once the throat pressure reduces below the liquid vapour pressure. All models produced positive values of throat pressure except the standard $k-\epsilon$ model, which resulted in negative values of pressure. According to bubble dynamic theory, Brennen (1995) and Plesset and Prosperetti (1977), cavitation should have occurred when the water pressure in the throat drops below the vapour pressure. As the standard $k-\epsilon$ model predicts negative pressure, cavitation should be observed. However, during tests performed in the cavitation cell, no bubble cloud was observed and no cavitation noise was heard under these simulation conditions. This implies that the standard $k-\epsilon$ model produces inaccurate results for these flow conditions where separation can be expected to occur in the diverging part of the nozzle.

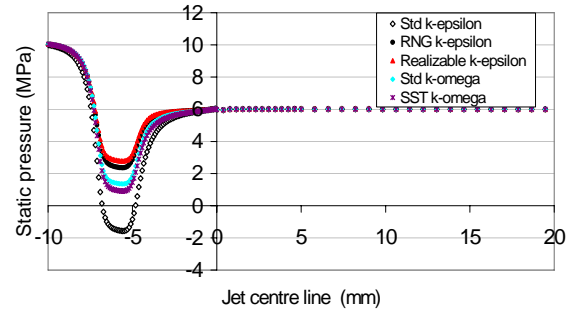


Figure 3: Pressure distribution along the jet centre line

As shown in Figure 4, except for the standard $k-\epsilon$ model, the velocity differences among the other four models are small in the nozzle throat ($x=-7.5 \sim -5$ mm) but the velocity differences among the models in the diverging portion ($x=-5 \sim 0$ mm) become significant. The RNG and the realizable $k-\epsilon$ models predicted nearly identical velocity profiles with the velocity values predicted on the centre line from $x = -3$ to $x = 3$ mm remaining nearly constant. This suggests a flow similar to that issuing from a converging nozzle into free space for which a potential core of up to four exit diameters in length is usually observed but in this case the potential core forms in the diverging section prior to exit from the nozzle. The standard $k-\epsilon$, standard $k-\omega$ and SST $k-\omega$ did not predict this feature.

From velocity vector plots in the diverging portion of the nozzle shown in Appendix A, it is seen that the RNG $k-\epsilon$ and $k-\omega$ models predicted the separation and recirculation of the jet flow close to the commencement of the diverging section while, the standard $k-\epsilon$ model predicted separation and recirculation only very near the exit. This is seen from the significant reverse flow at the wall of the diffuser for the first two models while almost stagnant flow is seen in the corresponding region for the $k-\epsilon$ model case.

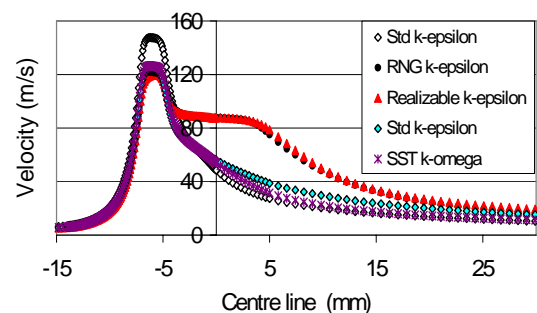


Figure 4: Velocity distribution on the centre line

In the five turbulence models being examined, the turbulent kinetic energy k is derived from a relatively exact transport equation. However, significant model approximations are required in the derivations of ϵ or ω transport equations. The RNG $k-\epsilon$ and realizable $k-\omega$ models share similarity of turbulent kinetic energy distributions and so do the standard and SST $k-\omega$ models. However, a significant difference exists between these two

groups of models. In the throat and the core of the flow within the divergent portion of the nozzle, the turbulent kinetic energy modelled by the RNG k- ϵ and the realizable k- ϵ models is very small (nearly zero). By contrast, the turbulent kinetic energy modelled by both k- ω models is very high in the throat, especially at the beginning of the throat part. These distinct differences can be seen in Figure 5. The radial distribution of turbulent kinetic energy given by the RNG and realisable k- ϵ models, Figure 6 are characteristic of a jet type flow.

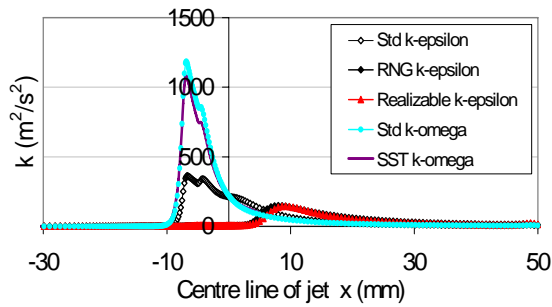


Figure 5: Turbulent kinetic energy distribution on the centre line

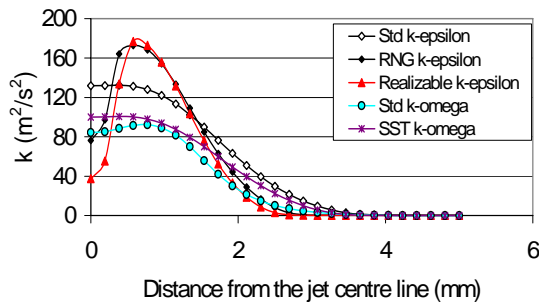


Figure 6: Radial distributions of turbulent kinetic energy at x=5mm

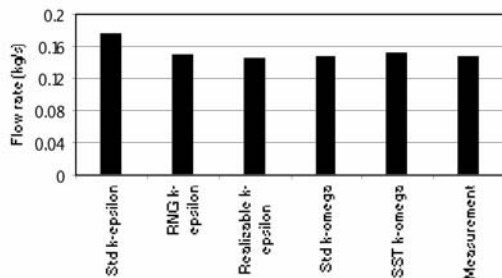


Figure 7: Comparison of CFD mass flow rates with measurement (pump pressure 10.2 MPa, cell pressure 6 MPa)

Flow measurements were conducted to test mass flow rates predicted by the different turbulence models for a nozzle the same size as that used in the CFD simulations. It is seen from Figure 7 that while the standard k- ϵ model predicted a much higher mass flow rate than the

measurement, the other four turbulence models predicted mass flow rate values close to the measurements. Although flow behaviour differs in the diverging section for the various models, total mass flow rate is almost unaffected except for the standard k- ϵ model.

ROTATING CYLINDER ELECTRODE

Preprocessing

The domain used for the 2D simulations consists of an inner circle of radius 10mm and an outer concentric circle of radius 70mm. An additional circular region of radius 15mm, defined as an interior surface in GAMBIT, was used to help with the refinement of the near-wall region. This geometry aimed to create a similar grid to that used in the DNS work (Hwang et al., 2005) - 128 cells in the azimuthal direction and 96 cells radially. In order to investigate the influence of the outer boundary condition on the wall shear stress results, simulations were also conducted for the two-dimensional grid with the outer boundary adjusted such that it had the same resolution as the inner rotating cylinder.

Solver Setup

For the majority of simulations, the inner and outer walls were set to no-slip and rotated around the moving fluid. The fluid was liquid water and all residuals were set to a level of 10^{-6} for convergence. A rotational velocity of 500rpm was used for all simulations.

The pressure discretization was set to body force weighted and all other discretization settings were set to second order upwind for each simulation.

Seven different RANS models were tested,

- i) the standard k- ϵ model,
- ii) the realizable k- ϵ model,
- iii) the renormalization group (RNG) k- ϵ model,
- iv) the standard k- ω model,
- v) the shear stress transport (SST) k- ω model,
- vi) the Reynolds stress model (RSM), and
- vii) the Spalart Allmaras model.

All k- ϵ model and RSM simulations used the enhanced wall treatment option to improve the near-wall results. The enhanced wall treatment option blends the linear and logarithmic laws of the wall so as to be applicable over the entire near-wall region.

In order to test the assumption of steady flow conditions, an unsteady standard k- ϵ simulation was run (with enhanced wall treatment). A second additional simulation with that turbulence model was run for a higher resolution at the outer boundary. The standard k- ω (with enhanced wall treatment), standard k- ω and Spalart Allmaras models were also tested on the original two-dimensional grid with the outer boundary condition set to a slip wall with no shear stress applied. In this way, the solution's dependence on the outer boundary condition was observed.

Unfortunately, difficulties were experienced with the RSM model, and converged solutions were not obtained despite reductions in the under-relaxation factors.

However, Pettersson et al. (1996) had previously shown that RSM models do not give accurate predictions of this type of flow and in particular gave values of wall shear stress which follow those predicted in the present work. Consequently, RSM modelling was not pursued further.

Results

Table 2 shows the wall shear stress results for the simulations. Calculation of the wall shear stress at the inner cylinder wall from the DNS found a value of 1.60 Pa. This is much larger than the data extracted from the turbulence model results. The Spalart-Allmaras model wall shear stress value in particular is quite low.

Model	$\tau_{w,inner}$ (Pa)	$\tau_{w,outer}$ (Pa)
Standard k- ϵ	0.918	5.93e-4
Realizable k- ϵ	0.935	4.31e-4
RNG k- ϵ	0.908	1.01e-3
Standard k- ω	0.782	5.52e-4
SST k- ω	0.787	1.24e-3
Spalart-Allmaras	0.555	5.88e-5
Standard k- ϵ (slip)	0.918	N/A
Standard k- ω (slip)	0.782	N/A
Spalart-Allmaras (slip)	0.555	N/A
Standard k- ϵ (refined)	0.915	8.53e-4

Table 2: Wall shear stress values

The velocity profiles from both outer wall boundary conditions (the standard non-slip wall and the slip wall) are practically identical and in the plots following the data is overlaid. The domain has quite a coarse resolution at the outer boundary, making the accuracy of the outer wall shear stress data (for the no-slip wall simulations) questionable. However, resolution of the outer boundary had almost no effect on the wall shear stress results, showing that the outer boundary condition has very little effect on the near-wall results and is as close to the DNS condition as possible. Time dependent simulations also had no effect on the final results.

Figure 8 plots the non-dimensional velocity profile in the near-wall region for the RANS simulations compared to the DNS data. The seven models all provide a very close match to the DNS in the near-wall region, but the k- ϵ and k- ω models simulated the logarithmic layer with more accuracy than the Spalart-Allmaras model and with a slope that compared reasonably well to the DNS over the entire domain. However, all models overpredicted the logarithmic layer velocity relative to the DNS data.

Figures 9 and 10 show the turbulence length and time scales respectively for the RANS simulations compared to the DNS data. There is a significant difference of one or more orders of magnitude amongst the turbulence model results and the DNS for both the length and time scales, although the various turbulence models compare well with each other. The exception to this is the shear stress transport k- ω model, which shows significant disagreement over the whole flow region. The transformation of ω to ϵ required a factor of C_μ to prevent the k- ω scales from being another order of magnitude smaller than the k- ϵ model results. This factor was taken as 0.09 in Equation 1.

$$\epsilon = C_\mu k \omega \quad (1)$$

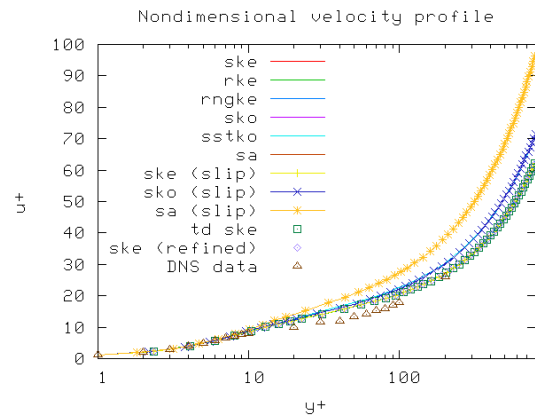


Figure 8: y^+ vs u^+ in the near-wall region

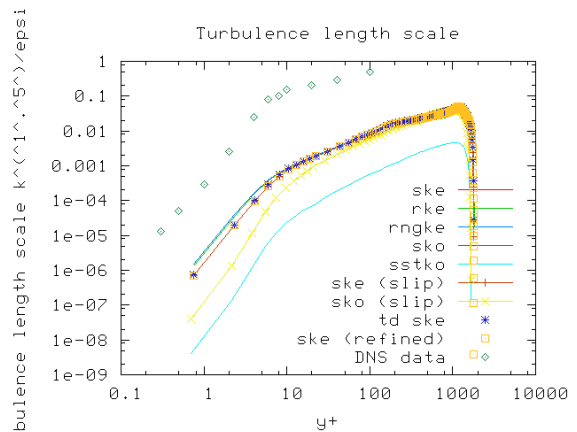


Figure 9: Turbulence length scale comparison

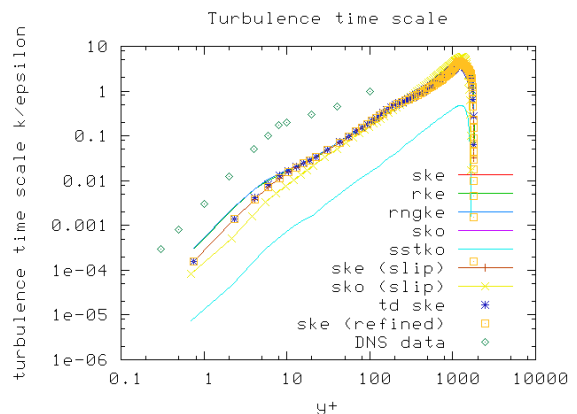


Figure 10: Turbulence time scale comparison

Figure 11 shows the near-wall turbulence kinetic energy profile for the RANS simulations compared to the DNS data. For the k- ϵ model, the turbulence kinetic energy peaks at approximately $y^+=15$ which is reasonably close to the peak at $y^+\sim 10$ that is predicted by the DNS data. The models also compare well to the DNS value of turbulence kinetic energy apart from some discrepancy with the standard k- ω model. The turbulence kinetic energy was normalized by the square of the friction velocity. Of the

turbulence models, the k-ε models compare best to the DNS results, especially in the near wall region.

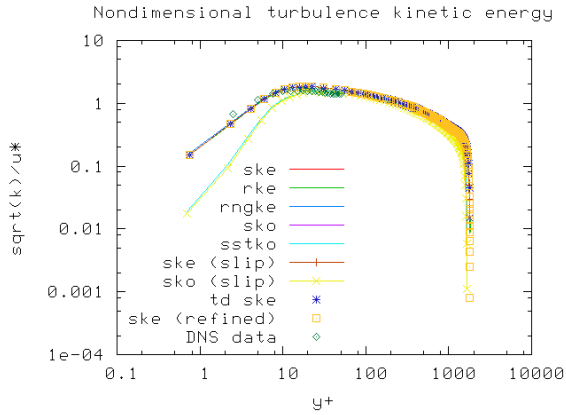


Figure 11: Nondimensional turbulence kinetic energy comparison

Figure 12 shows the near-wall turbulence dissipation rate profile for the RANS simulations compared to the DNS data. The models converge to the DNS solution further from the wall, but overestimate the turbulence dissipation rate in the near-wall region. Directly at the wall, ϵ is underestimated by the standard k-ω model.

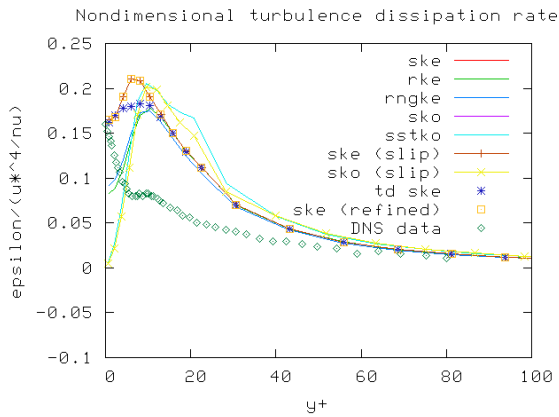


Figure 12: Nondimensional turbulence dissipation rate comparison

For the standard k-ε model, the model data extracted from FLUENT is not the true value of ϵ that the DNS provides. The following transformation was necessary to compare the k-ε values with the DNS,

$$\epsilon = \epsilon^* + \epsilon_0 \quad (2)$$

where $\epsilon_0 = 2\nu \left(\frac{\partial \sqrt{k}}{\partial y} \right)^2$ and $\epsilon^* = \nu \left(\frac{\partial u_i}{\partial x_j} \frac{\partial u_i}{\partial x_j} \right)$. The value of ϵ plotted in the Figure 12 was normalized by $(u^*)^4 / \nu$.

The error in the turbulence dissipation rate in the wall region is the most likely cause of the shifts visible in the turbulence length and time scale plots. Otherwise, the results show a very good approximation to the DNS data,

with the enhanced wall treatment k-ε models performing slightly better than the k-ω models.

CONCLUSION

Water flows through a small diameter converging-diverging nozzle were simulated with five different turbulence models. Of the five two-equation turbulence models, the standard k-ε model is inaccurate because it cannot properly model the separation and recirculation of the flow in the divergent section which leads to a consequent overprediction of the velocity in the throat of the nozzle. The RNG k-ε, realizable k-ε, standard k-ω and SST k-ω models produce similarly shaped profiles of pressure but with significant differences in magnitude. Velocity profiles for the remaining two k-ε based models give a prediction that differs significantly from that of the two k-ω based models due to the quite different behaviours in the diverging section of the nozzle. All except the standard k-ε model give good agreement with measured mass flow rate.

Although the standard and SST k-ω models give reasonable flow patterns (separation and recirculation) in the divergent section, they give rise to quite different turbulent kinetic energy levels to those predicted by the RNG k-ε model and the realizable k-ε model. This together with the different pressure levels in the nozzle can lead to a significant effect on predictions of cavitation onset and hence cutter performance.

For the rotating cylinder electrode, the enhanced wall treatment option produced the best results for the k-ε models while the k-ω models performed well with the standard options. It was found that the Spalart-Allmaras model did not model the logarithmic layer of the flow as well as the other models. The turbulence length and time scales for the simulations were significantly affected by the overestimation of the turbulence dissipation rate near the wall. Wall shear stress values near the inner cylinder wall were underestimated by all models.

In order to better match the DNS outer boundary condition, some simulations were run with the outer wall set to a slip wall with no shear stress applied. As the results from the non-slip outer boundary showed very small wall shear stress values at the outer wall, very little difference was visible between the two outer boundary settings. Refinement of the outer boundary grid and time dependent simulation also proved to have little overall effect. Therefore, the outer boundary condition did not overly affect the results at the inner boundary layer.

ACKNOWLEDGEMENT

The work on the converging-diverging nozzle was conducted within the Step Change Mining Technologies Program of CRC Mining (formerly CMTE). Industry support from BHP Billiton-Mitsui Alliance and Anglo Coal Australia is gratefully acknowledged.

REFERENCES

BRENNEN, C.E., (1995), *Cavitation and bubble dynamics*, Oxford, New York.

ERDMANN, F., (1978), "A study of the effect of nozzle configuration on the performance of submerged water jets", *4th International Symposium on Jet Cutting Technology*, Canterbury, England, April 12-14.

GABE, D., (1974), "The rotating cylinder electrode", *Journal of Applied Electrochemistry*, **4**(2), 91-108.

GABE, D. and WALSH, F., (1983), "The rotating cylinder electrode: a review of development", *Journal of Applied Electrochemistry*, **13**(1), 3-21.

HWANG, J., YANG, K., and BREMHORST, K., (2005), "Direct numerical simulation of turbulent flow around a rotating circular cylinder", *Proceedings of 2005 ASME Fluids Engineering Division Summer Meeting, FEDSM2005*, 2195-2200.

LICHTAROWICZ, A., PEARCE, I.D. and LAMPARD D., (1999), "Applications of cavitation to water jet technology: performance of long orifice nozzle with cavitating flow", *International Symposium on New Applications of Water Jet Technology*, Ishinomaki, Japan, October 19-21.

MEYER, T., CARNAVAS, P., ALEHOSSEIN, H., HOOD, M., ADAM, S., and GLEDHILL, M., (1999), "The effect of nozzle design on the erosion performance of cavitating water jets", *International Symposium on New Applications of Water Jet Technology*, Ishinomaki, Japan, October 19-21.

OKUMURA, K., IINO, W., MATSUKI, K. and KUME, S., (1999), "Fundamental study on removal of geothermal scales with high-pressure water jets", *International Symposium on New Applications of Water Jet Technology*, Ishinomaki, Japan, October 19-21.

PETTERSSON, B., ANDERSSON, H., and HJELM-LARSEN, Ø, (1996), "Analysis of near-wall second moment closures applied to flows affected by streamline curvature", in W. Rodi and G. Bergeles (ed.) *Engineering Turbulence Modelling and Experiments 3*, Elsevier, 49-58.

PLESSET, M.S., and PROSPERETTI, A., "Bubble dynamics and cavitation", *Ann. Rev. Fluid Mech.*, **9**, 145-185.

QIN, Z., (2004)., *Investigation of the cavitation mechanism and erosion of submerged high-pressure water jets*, PhD thesis, The University of Queensland, Brisbane, Australia.

SILVERMAN, D., (1988), "Rotating cylinder electrode - geometry relationships for prediction of velocity-sensitive corrosion", *Corrosion - NACE*, **44**(1), 42-49.

TERASAKI, N., FUJIKAWA, S., TAKASUGI, N., HAYAMA, S. and SUGINO, Y., (1999), "Improvement of machining performance of submerged water jet by cavitation", *International Symposium on New Applications of Water Jet Technology*, Ishinomaki, Japan, October 19-21.

YANAIDA, K., (1985), "Water jet cavitation performance of submerged horn shaped nozzles", *Proc. 3rd US Water Jet Conf.*, Pittsburgh, Pennsylvania, 336-349, May.

APPENDIX A

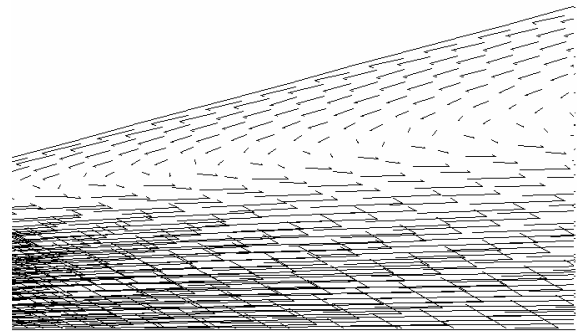


Figure A1: Vector field- RNG k-ε model

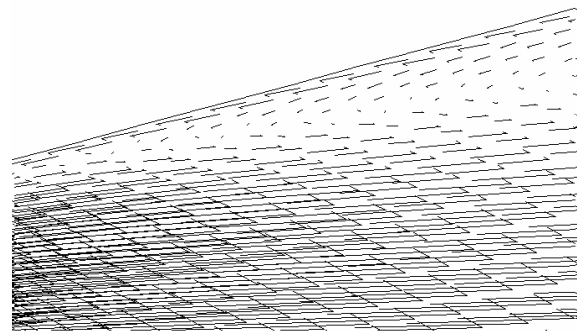


Figure A2: Vector field - standard k-ω model

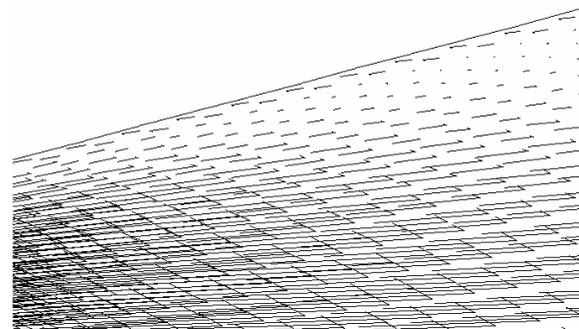


Figure A3: Vector field - standard k-ε model